ACS Catalysis

pubs.acs.org/acscatalysis Research Article

Dopant-Dependent Boron Arrangement and Chemistry of Metal Boride Surface

Zisheng Zhang and Frank Abild-Pedersen*

Cite This: ACS Catal. 2026, 16, 1729−1737 Read Online

ACCESS | Metrics & More | Article Recommendations | Supporting Information

ABSTRACT: Borides, an emerging family of materials with rich and diverse stoichiometries and structures, have exhibited boron-dependent catalytic properties where boron instead of the metal governs the surface chemistry. However, boron motifs are inherently polymorphic and can be prone to fluxional rearrangement, making it difficult to resolve or control the active site structures. Here, we show that metal doping can direct the arrangement of surface boron and thereby tune the accessible surface boron configurations. Using extensive global optimization searches combined with ab initio thermodynamics, we identify synthesizable surface phases across a range of surface boron stoichiometries. The resulting surfaces display a wealth of geometric and electronic structures, whose origins are traced to dopant-stabilized boron rearrangements. These nonuniform multisite surfaces bind different adsorbates through distinct modes, thus making it impossible to comply with conventional catalysis models such as scaling relations. We further demonstrate that multiobjective searches can efficiently navigate this chemical space and reveal candidates that deliberately escape traditional activity-selectivity-durability trade-offs. The results establish a promising catalyst system with highly controllable reactivity enabled by dopant-dependent boron arrangements, and provide a generalizable workflow for other fluxional catalytic systems.

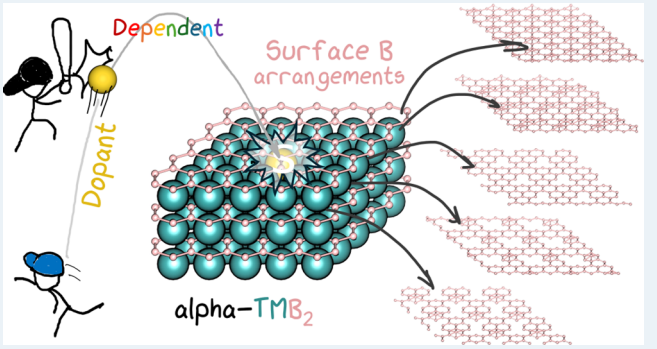

KEYWORDS: *boride, doping, grand canonical ensemble, global optimization, surface phase diagram, surface rearrangement, electrocatalysis, multi-objective Design*

INTRODUCTION

Boron stands out within the periodic table due to its unique electronic structure and valence count, affording unusual chemical bonding modes rarely seen in other main group elements.[1] This underlies boron's ability to form a large variety of stable and metastable configurations in elemental polymorphs, inorganic clusters, and solid-state boride compounds.[2,3] The structural diversity inherent in boron-containing materials directly translates into a broad distribution of physical properties and chemical reactivity.[4] Different arrangements of boron allow for distinct chemical bonding and local environments, impacting how these sites behave and interact with other chemical species or respond to external stimuli.[5]

In catalysis, borides are emerging as a promising model system due to their boron-dependent reactivity: boron, rather than the other element in borides, has been identified as the active species in various important thermal and electrocatalytic reactions including oxidative dehydrogenation of light alkanes,[6] hydrogen evolution,[7] and CO_2 reduction reactions.[8] Additionally, the local chemical environment and surface arrangement of boron atoms have been found to be key factors dictating catalytic reactivity.[9] Consequently, engineering the surface chemistry of borides essentially amounts to manipulating surface boron stoichiometry and arrangements to access the richness of local environments seen in boron allotropes and clusters.[10]

Metal doping, as a classic materials engineering strategy, has been widely applied to improve various transition metal compound catalyst systems such as chalcogenides or pnictogenides.[11,12] However, in the realm of boron chemistry, doping has seen the most progress in isolated boron clusters.[13] In contrast, explorations of metal doping effects in bulk solid-state boride materials remain comparatively less extensive and systematic. Furthermore, the surface of borides exhibits significant fluxionality, often leading to dynamic surface evolution or dramatic surface reconstructions.[10,14,15] This makes the investigation of doping effects especially challenging, as the boron arrangement can strongly distort or even

Received: November 18, 2025
Revised: December 19, 2025
Accepted: December 23, 2025
Published: January 5, 2026

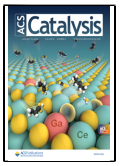

https://doi.org/10.1021/acscatal.5c08265
ACS Catal. 2026, 16, 1729−1737

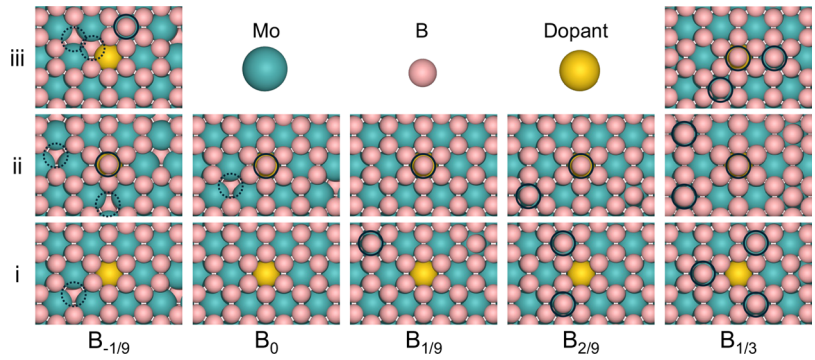

Figure 1. All low-lying surface boron configurations at different stoichiometries. Each column corresponds to global minimum configurations (i, ii, iii) of a surface boron stoichiometry.

rearrange when dopants are introduced, unlike the simpler site substitutions in most other compounds. Hence, understanding how various dopants influence the resulting geometric and electronic structures of boride surfaces remains a unique and promising challenge.

In this work, we explore the chemical space of nonstoichiometric diboride surfaces with various dopants through grand canonical global optimization minima searches at the ab initio level. We find that multiple distinct surface boron arrangements can be present for each surface stoichiometry, with the configuration being highly dependent on the dopant. Synthesizable configurations are predicted from grand canonical surface phase diagrams derived from ab initio thermodynamics. We analyze the great diversity of geometric and electronic structures induced by doping, as well as their correlation with elemental properties of the dopants. The diverse and heterogeneous surface boron sites afford different binding modes for different adsorbates, inhibiting its compliance with common catalyst design principles such as linear scaling relations. Such an expansive reactivity space can be explored by multiobjective optimization methods to identify promising candidates considering multiple properties. We aim to highlight the surprising structural diversity that arises from simple doping and its catalytic consequences, and to provide a general workflow for exploring the multidimensional reactivity space of nonstoichiometric reconstructed catalyst surfaces.

RESULTS AND DISCUSSION

Predicting Synthesizable Surface Phases

In this study, we choose the B-terminated (100) facet of α-phase molybdenum diboride (α−MoB_2) as the parent system, as it has been reported to have high activity toward the hydrogen evolution reaction, with the reactivity originating from the hexagonal boron layer within.[7,16] For doping, we consider the substitution of one subsurface Mo atom by elements in groups IV to VIII in periods 4 to 6, except for Tc which does not have any stable isotope. This model represents the dilute doping limit where the layered boron structure is preserved in the bulk and at the surface termination. This allows us to better probe the extent of structural changes that can be induced by minimal doping, and to avoid the otherwise complication of phase segregation at higher doping ratios.

Our first step is to identify the surface phases that can be practically synthesized upon doping. Due to boron's fluxionality and tendency to reconstruct,[17] we could not assume a fixed lattice as in the bulk structure. The usually high variation in the boron-to-metal ratio in reagents[18] also prompts us to consider B-rich and B-poor surface stoichiometries. To account for these complexities, we perform grand canonical global optimization minima searches at the density functional theory level, using our GOCIA code.[19]

For *each* dopant system, we sample 1000 surface configurations with surface B coverage (θ_B) between −2/9 and 1 ML (B-poor to B-rich relative to the stoichiometric termination) and obtained about 300 unique minima structures that are symmetrically nonequivalent. Considering the usually high temperatures involved in boride nanocrystal synthesis,[5,20] we only consider the global minimum surface phase for each surface stoichiometry. As can be seen in Figure 1, there exist multiple surface boron arrangements for each surface stoichiometry: At the stoichiometric termination (denoted as B_0), the surface boron can either arrange in a hexagonal lattice as in the α-diboride bulk (configuration (i) or to displace one of the B atoms to occupy the center of a neighboring hexagon unit (configuration (ii), forming an adatom-vacancy pair. The visualization of the larger-scale periodic pattern of surface boron layer is shown in Figure S2. At B coverage of −1/9 ML (denoted as $B_{-1/9}$), configuration ii (denoted as $B_{-1/9}$-ii) has one vacancy per simulation box located in the center of the hexagon unit above the dopant or its adjacent one, respectively. Configurations $B_{-1/9}$-i and $B_{-1/9}$-iii, however, prefer to displace a surface B atom to form two vacancies and one adatom, similar to the case in B_0-ii. For the B-rich cases of $B_{1/9}$, $B_{2/9}$, and $B_{1/3}$, there are no more vacancies in the global minima configurations, and variations arise from the relative arrangement of adatoms to the dopant (despite that some of them share the same surface boron pattern). Some configurations prefer to have adatoms atop the dopant ($B_{1/9}$-ii, $B_{2/9}$-ii, $B_{1/3}$-ii, $B_{1/3}$-iii), whereas some prefer to have them in the adjacent hexagonal ring or the second adjacent one ($B_{1/9}$-i, $B_{2/9}$-i, $B_{1/3}$-i).

Different dopants lead to different global minimum configurations of the surface boron at each θ_B. For example, surface boron would prefer configuration ii in the presence of Cr, Mn, Fe, or Ru dopants, while configuration i would be preferred for other dopants. The preference for surface boron configuration is dependent on the dopant but is not identical across the stoichiometries. In Table 1, we summarize the global minimum configurations (shown in Figure 1) identified for each dopant.

The condition of boride nanocrystal synthesis typically involves a controlled B-rich environment and high temperatures, i.e., the system is a well equilibrated grand canonical ensemble with respect to boron, and the system can always

https://doi.org/10.1021/acscatal.5c08265
ACS Catal. 2026, 16, 1729−1737

Table 1. Global Minimum Surface Boron Configurations of All Doped Terminations with Varying Surface Boron Stoichiometries[a]

dopant	$B_{-1/9}$	B_0	$B_{1/9}$	$B_{2/9}$	$B_{1/3}$
Ti	~~i~~	i	i	~~i~~	i
V	~~iii~~	i	ii	~~ii~~	i
Cr	~~ii~~	ii	ii	ii	ii
Mn	~~ii~~	ii	ii	~~ii~~	iii
Fe	~~ii~~	ii	ii	ii	~~i~~
Zr	~~i~~	i	i	~~i~~	i
Nb	~~i~~	i	i	~~i~~	i
Mo	~~i~~	i	i	~~ii~~	ii
Ru	i	~~ii~~	ii	ii	ii
Hf	~~i~~	i	i	~~i~~	i
Ta	~~i~~	i	i	i	i
W	~~i~~	i	i	i	~~i~~
Re	i	~~i~~	ii	ii	ii
Os	i	~~i~~	ii	ii	ii

[a]The inaccessible phases are marked by strike-out lines.

equilibrate to the thermodynamic global minimum surface phase which depends on the dopant and μ_B.[10] Therefore, the appropriate thermodynamic metric is the grand potential Ω_B approximated as

$$\Omega_B = G_{nonstoi.} - G_{stoi.} - n_B\mu_B \quad (1)$$

where G is the Gibbs free energy, n_B is the difference in the number of extra surface B atoms referenced against the stoichiometric termination, and μ_B is the chemical potential of boron corresponding to the condition of synthesis. By calculating Ω_B and formation energy E_{form} for all surface phases at varying synthesis-relevant μ_B, we can construct a surface phase diagram and identify the most stable surface phase within the grand canonical ensemble, for each dopant of study and any specific μ_B. This informs which surface stoichiometries are thermodynamically accessible during synthesis according to ab initio thermodynamics, with the accessible ones marked by thicker colored lines in Figure 2. Many surface stoichiometries become thermodynamically inaccessible because they are less stable than neighboring stoichiometries within the grand canonical ensemble; for example, the $B_{2/9}$ phase in the undoped system is always outcompeted in free energy. We mark such inaccessible phases using strike-out text in Table 1. Importantly, being a local minimum at a given stoichiometry does not guarantee accessibility under synthesis-relevant conditions, as multiple stoichiometries can coexist and compete on the same grand canonical free-energy scale. The structures of all accessible surface phases are provided in Figures S3–S7. From the thermodynamic perspective of dispersed dilute doping, early transition metal dopants (Ti, Zr, Hf, V, Ta) could be more easily incorporated into the Mo diboride host than middle transition metal dopants (Mn, Re, Fe, Ru, Os), but the incorporation of all these dopants is thermodynamically favorable relative to elemental forms. Note that, at a higher doping ratio, alternative processes such as phase segregation, in-bulk (instead of near-surface) redistribution, or the formation of alternative compounds may become relevant. These effects are beyond the scope of the present analysis, which focuses on near-surface dilute doping scenario motivated by available experimental evidence where well-mixed diboride samples are prepared under a doping ratio of 0.3.[4]

We then investigate whether the surface boron would rearrange in the synthesized catalysts, which is common in some metal diborides such as MgB_2.[17] The surface phase transition from configuration i to ii for the stoichiometric surface, as a representative scenario, is studied by nudged elastic band (NEB) calculations for all dopants of study. In Figure S8, we found that the transition must proceed by migration of a B_2 dimer, and the barriers are quite high for all dopants, between 1.6 and 3.1 eV. Vibrational analyses and ab initio molecular dynamics simulations also confirm the stability of the as-formed surface phases (Supplementary Note S2). Hence, it should be safe to assume that the surface boron configurations would not easily rearrange at ambient temperature on their own after the catalyst has been synthesized. This also means that the metastable surface phases (gray lines in Figure 2) may also be prepared, via nonequilibrium synthesis techniques such as plasma or quenching, and they can remain stable at room temperature to be potentially useful.

Origin of Dopant-Dependent Surface B Arrangement

The dependence of surface boron arrangement on the dopant is intriguing. To systematically investigate this dopant-dependent behavior, we take the configurations i and ii of the stoichiometric surface as representatives of the pristine and

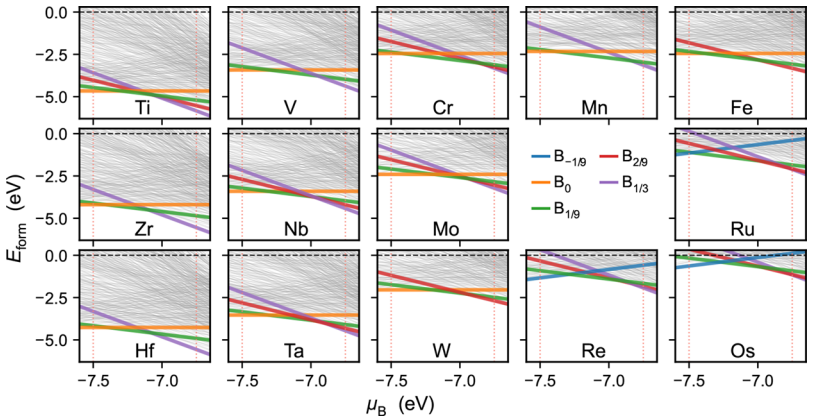

Figure 2. Surface phase diagrams of surface B arrangement as a function of chemical potential of B for all dopants. The pink dotted lines mark the lower and upper limit of chemical potential of B in synthetic conditions (from boron oxide to elemental boron).

https://doi.org/10.1021/acscatal.5c08265
ACS Catal. 2026, 16, 1729−1737

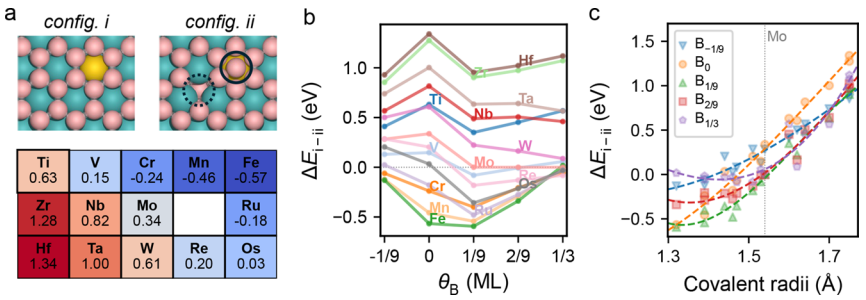

Figure 3. Analysis of the energy difference to go from configuration i to ii, ΔE_{i-ii}, of each surface boron stoichiometry. (a) Top views of the configurations i and ii, and the dopant table colored by the ΔE_{i-ii} of B_0 surface phases. Color code: Mo: dark cyan, B: pink, dopant: yellow. Warmer or cooler colors in the lower panel indicate configuration i or ii being favored, respectively. (b) The ΔE_{i-ii} at varying surface boron stoichiometries for all dopants studied. (c) Correlation between ΔE_{i-ii} and the covalent radii of the dopants.

symmetry-broken case, and calculate the energy difference between them ($\Delta E_{i-ii} = E_{ii} - E_i$) for all dopants studied.

In the color-filled periodic table block in Figure 3a, there is a rough trend, where heavier and earlier transition metals (Ti, Zr, Hf, V, Nb, Ta, Mo, W, Re, Os) tend to prefer configuration i over ii, whereas, lighter and later transition metals (Fe, Ru, Mn, Cr) exhibit the opposite preference. This trend largely persists for other surface stoichiometries, as shown by the variation of the energy gap between configurations i and ii (ΔE_{i-ii}) in Figure 3b. For the B-rich cases ($B_{1/9}$ to $B_{1/3}$), the surface B vacancy is absent, and the configurational preference reflects whether the extra B adatom prefers to reside atop or in close proximity to the dopant site. Thus, this can be viewed as a matter of affinity between the dopant atom and the additional B adatoms, within the hexagonal lattice of surface B.

To further understand the origin of this configurational preference, we examined correlations between ΔE_{i-ii} and various atomic properties including covalent radii, electronegativity, cohesive energy, and Bader charge of the dopant atom (Figure S10). Among them, the covalent radius shows the best overall agreement with an approximate linear correlation, suggesting the primarily geometric origin of the stability trends. For the stoichiometric termination (B_0), ΔE_{i-ii} scales nearly linearly with the covalent radius (orange circle markers in Figure 3c), indicating a predominantly geometric origin. Larger dopants crowd the local lattice, promoting corrugation and favoring formation of the B_7 motif by hosting an additional atop B. Smaller dopants, by contrast, interact more weakly with the B_6 ring and stabilize the original lattice, thereby repelling B adatoms from its atop position. The competition between these two stabilization mechanisms depends linearly on the covalent radius for the stoichiometric termination and determines the configurational preference of surface B arrangements.

Figure S11 shows that, as the surface becomes more B-rich, the linear region shortens due to stronger intrinsic local crowding. The ΔE_{i-ii} flattens as the covalent radius decreases, suggesting that surface B becomes insensitive to very small dopants. Larger compositional deviations from the stoichiometric termination yield a smaller linear region and a larger flattening region. At $B_{1/3}$, the onset of flattening appears as early as the covalent radius of Mo (the parent system). By comparison, the B-poor surface also shows some nonlinear behavior due to intrinsic lattice distortion, but lacks a pronounced flattening region.

Note that we also examined the atomic charges of the dopants and their local environments (Figures S26–S28), which exhibit a similar trend but a weaker correlation with ΔE_{i-ii} (Figure S10). This suggests that the dopant-dependent configuration of surface B is governed primarily by dopant size and its fit within the hexagonal B lattice of the parent bulk. The minor deviations from a linear trend reflect some electronic interactions beyond simple size and electrostatic effects. However, the subtleties of chemical bonding in metal–boron systems are notoriously difficult to probe and represent using a few simple metrics[21] in a high-throughput screening study.

Structural Diversity of Surface B Moieties

The dopant-dependent surface boron arrangements are accompanied by varying degrees of structural distortion in the surface B layer. In Figure 4, the *x*-axis denotes the average

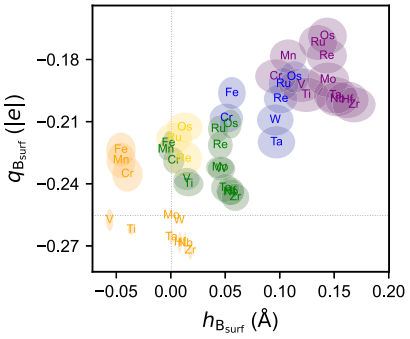

Figure 4. Structural distortion and charge variation of surface B atoms for different surface stoichiometries and dopants. $B_{1/9}$, B_0, $B_{1/9}$, $B_{2/9}$, and $B_{1/3}$ are colored by yellow, orange, green, blue, and purple, respectively. The width and height of the eclipses represent the scaled standard deviation in height and Bader charge of surface boron atoms, which reflects the multimodal nature and relative distribution breadth of the site properties. The standard deviations of heights and charges are scaled by 0.25 and 0.1 for visual clarity, respectively.

height of surface B atoms relative to the pristine stoichiometric B termination. The full plot with error bars in exact scales and the tabulated data are provided in Figure S29 and Table S1, respectively. In general, B-poor and B-rich surfaces exhibit lower and higher surface B heights, respectively. The relative error ranges (scaled standard deviations of the surface B height) further reveal stronger surface corrugation effects. These geometric features have direct electronic consequences: B-rich and B-poor surface phases display a broad distribution of atomic charges, and the dispersion widens as the surface deviates further from the stoichiometric case, driven by the increased surface concentration of adatoms.

https://doi.org/10.1021/acscatal.5c08265
ACS Catal. 2026, 16, 1729–1737

The larger dispersion of surface charge originates from distinct local environments in different surface B arrangements. In Figure 5, the local environments of surface B atoms (from the surface phases in Figure 1) are classified into three types: pristine sites, corresponding to defect-free hexagonal rings; vacancy sites, formed by the removal of one B atom from the hexagonal lattice; and adatom sites, located atop the center of an intact hexagonal B_6 ring.

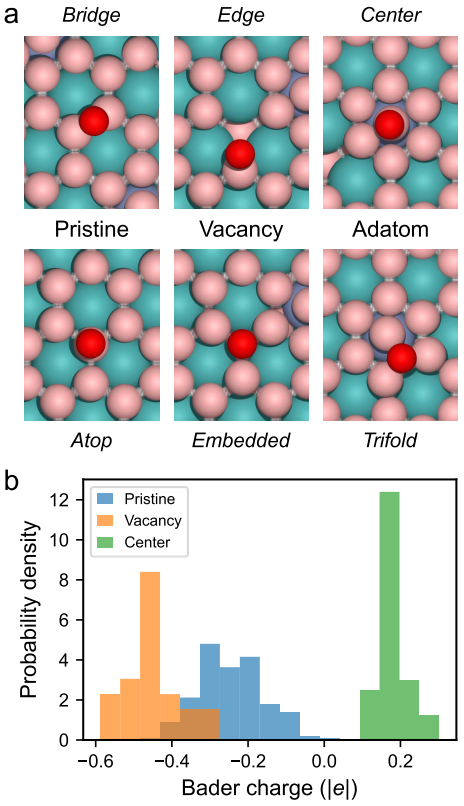

Figure 5. Classification of surface boron motifs. (a) The configurations and adsorbate binding modes and (b) the distribution of Bader charge for surface B atoms in different local environments.

Beyond their structural differences, the three site types also diverge in charge states. Figure 5 presents the distribution of Bader charges of surface B atoms across different site types. Pristine sites are mildly anionic, with an average Bader charge of about −0.2 |e|. Vacancy sites are more strongly anionic, averaging −0.5 |e|. In contrast, adatom sites are mildly cationic, with an average Bader charge of approximately +0.2 |e|.

Even within the same site type, variations in second-sphere environments and local structural distortions induced by different dopants and Ω_B further modify the charge distribution within the surface B layer. This gives rise to an ensemble of heterogeneous sites characterized by a broad distribution of charge states and, consequently, a wide range of distinct local chemical properties.[22]

Uncorrelated Adsorption Modes and Energetics

To further evaluate the catalytic consequences of dopant-dependent surface B arrangements, we compute the adsorption energetics of various adsorbates. Due to the high degree of heterogeneity in surface boron sites (*vide supra*), as well as boron's capacity to form diverse local motifs and binding modes, we perform extensive global optimization to identify the most stable adsorption configurations for each adsorbate−surface phase pair. No binding modes or graph representations are prescribed during the sampling, thereby allowing for the discovery of unconventional binding modes. Between 10 and 50 unique binding configurations are identified per adsorbate−surface phase pair, which can be broadly classified into six groups, as illustrated in Figure 5a. In the following discussion, only the most stable binding mode is used to evaluate adsorption energetics.

We begin with the hydrogen evolution reaction (HER), for which the parent system MoB_2 has been reported to exhibit exceptional activity. From the sampling of H adsorption, we find that H preferentially occupies the center mode atop the adatoms, and the bridge mode on pristine sites when adatoms are absent. Both modes overbind H, with adsorption energies $E_{ads}(H)$ spanning from −0.75 to −0.51 eV for the bridge mode, and from −0.52 to −0.41 eV for the center mode. In addition to H adsorption, we also evaluate OH adsorption, which provides insight into the susceptibility of surface B to oxidative dissolution via hydroxylation. Unlike H, OH can also occupy the edge mode at vacancies. For surface phases where both H and OH bind via the same mode: either bridge (green cluster) or center (orange cluster). As a result, a near-linear relationship emerges between $E_{ads}(H)$ and $E_{ads}(OH)$, with similar slopes but distinct intercepts. In contrast, on certain surface phases, H and OH adopt mismatched binding modes, such as H in the bridge mode and OH at the edge (blue cluster), or H in the bridge mode and OH in the center (red cluster). These mismatched adsorption modes arise from differing chemical bonding of the surface boron moieties, resulting in an uncorrelated scattering of adsorption energetics. Consequently, the overall trend is not governed by a single scaling relation (which assumes unchanged binding modes), but rather by an aggregate of multiple linear and uncorrelated clusters. The accessible energy range for HER, induced by very dilute doping through surface boron rearrangements, can reach up to 0.5 eV.

Next we examine the impact of surface B arrangements on the CO_2 reduction reaction (CO_2RR). Here, the key descriptors are $E_{ads}(H)$ and $E_{ads}(CO)$.[23] Similar to HER, H and CO adsorption exhibit no overall correlation, owing to their decoupled binding motifs. The accessible energy range for CO adsorption reaches 0.8 eV, ranging from the weakest binding at bridge sites to the strongest binding at edge sites.

Motivated by previous reports highlighting orbital symmetry alignment between the π^* orbitals of N_2 and boron frontier orbitals,[24,25] we also evaluate N adsorption, using gas-phase N_2 as the reference. This descriptor reflects the propensity for N_2 activation. We find an even broader energy range of 1.6 eV for N adsorption, with the embedded mode providing the strongest binding and the bridge mode the weakest.

For the nitrogen reduction reaction (NRR), high activity requires balancing N_2 activation with NH_3 desorption, a relationship often correlated on metallic surfaces. On boron-rearranged surfaces, however, adsorption energetics are largely uncorrelated, mirroring the cases of HER and CO_2RR. Due to the fundamentally distinct bonding characteristics of *N and *NH_3 on the diverse surface motifs afforded by boron, the binding modes of N and NH_3 never coincide on any studied phase. On pristine surfaces where N binds via the bridge mode, NH_3 favors the atop mode. On surfaces with adatom-vacancy pairs, N stabilizes at the embedded vacancy site, while NH_3 adsorbs at the edge. On B-rich surfaces, N preferentially binds in a trifold mode at adatom sites, while NH_3 stabilizes in the

https://doi.org/10.1021/acscatal.5c08265
ACS Catal. 2026, 16, 1729−1737

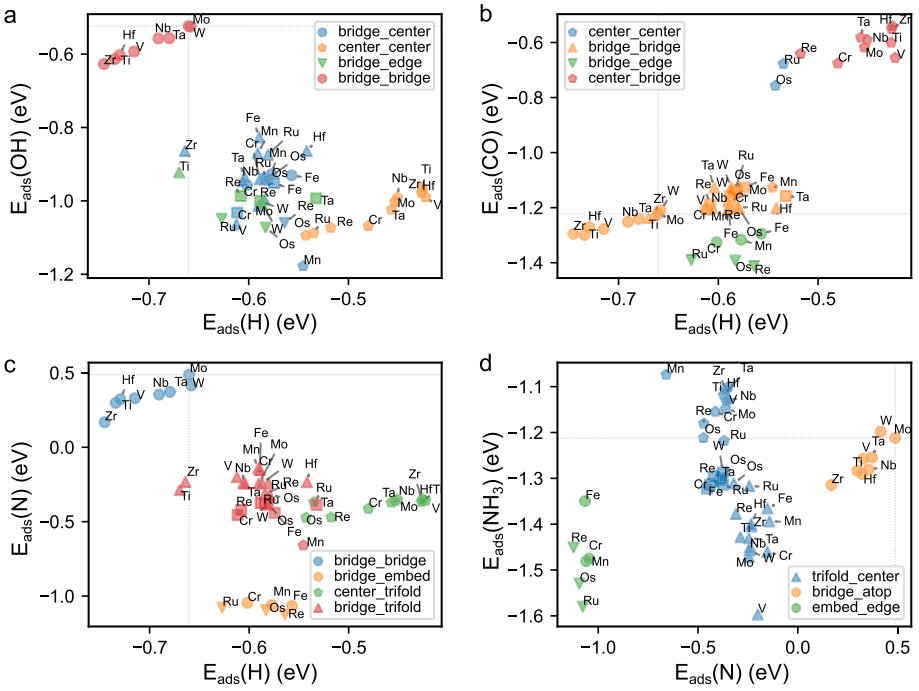

Figure 6. Deviation from linear scaling relations due to surface boron configuration-dependent binding modes. The reactions are (a) hydrogen evolution reaction, (b) CO_2 reduction reaction, and (c) selective and (d) active nitrogen reduction reaction. Marker code: triangle: $B_{-1/9}$, circle: B_0, inverted triangle: $B_{1/9}$, square: $B_{2/9}$, and pentagon: $B_{1/3}$. Coloring indicates the binding mode combinations as in each legend. The black text next to each marker indicates the dopant.

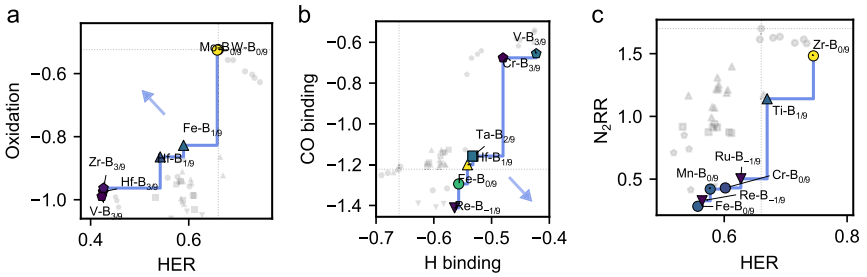

Figure 7. Pareto searches of doped diborides for (a) alkaline hydrogen evolution reaction, (b) selective CO_2 reduction reaction, and (c) selective N_2 reduction reaction. A rough search direction is labeled by an blue arrow in each plot.

center mode atop the adatom. The electronic origins of these binding preferences yield nearly decoupled energetics between the embedded-edge cluster (orange) and the trifold-center cluster (green): E_{ads}(N) remains nearly constant, whereas E_{ads}(NH_3) varies substantially. It is a similar case for larger adsorbates such as *NNH which adopts slightly different side-on bidentate binding mode over vacancy, pristine, and adatoms sites (Figure S31). Hence, we expect there to be more drastic decorrelating behaviors for larger and more flexible poly atomic adsorbates, which could provide a greater design space for complex multistep reactions.

Multiobjective Design of Boride Catalysts

Inspired by the energy range accessible through surface boron rearrangements induced by very dilute doping, we next explore the space of different dopants and surface B stoichiometries in search of promising catalytic candidates. The key advantage of this system lies in the heterogeneity of surface sites and the resulting decoupling of adsorption energetics. To leverage this property, we design a Pareto multiobjective search scheme (Supplementary Note 3) aimed at optimizing multiple adsorption-energy-based metrics within the defined chemical space.

We first focus on identifying HER catalysts with both high activity (using $|\Delta G_{ads}(H)|$ as the descriptor) and resistance to oxidative dissolution (using E_{ads}(OH) as the descriptor). In Figure 7a, the Pareto frontier and the corresponding optimal candidates are highlighted. For acidic HER, where hydronium serves as the primary proton source, V-, Zr-, and Hf-doping in B-rich surfaces markedly enhances HER activity. In contrast, for neutral or alkaline HER—where proton supply originates from water dissociation—W- or Fe-doped stoichiometric and B-poor surfaces prevent hydroxylation of surface B while retaining high HER activity.

For CO_2RR, both activity and selectivity are jointly dictated by the binding strength of H and CO. To promote selectivity toward multicarbon products, the design principle is to weaken H binding while strengthening CO binding.[23] Figure 7b presents the Pareto frontier and optimal candidates with E_{ads}(H) and E_{ads}(CO) as the descriptors. Relative to the parent system, the Re-doped B-poor surface strengthens CO binding by 0.19 eV while weakening H binding by 0.10 eV. V-doped B-

https://doi.org/10.1021/acscatal.5c08265
ACS Catal. 2026, 16, 1729−1737

rich surfaces, on the other hand, weaken both CO and H binding by 0.24 and 0.59 eV, respectively. Under alkaline conditions, Fe-doped stoichiometric surfaces and Ta-doped B-rich surfaces exhibit weakened H binding while also demonstrating increased resistance to hydroxylation. Although all Pareto-optimal candidates remain comparable to Cu in CO_2RR activity, the energy range accessible through dilute doping is nevertheless highly promising.

For the nitrogen reduction reaction (N_2RR), the optimal catalyst must balance N_2 activation and NH_3 desorption in accordance with the Sabatier principle.[26,27] As shown in Figure 6d, most boride surface phases readily activate dinitrogen but tend to overbind NH_3. We therefore define an N_2RR descriptor as $|E_{ads}(N) - E_{ads}(NH_3)|$, which reflects the balance between reactant activation and product desorption. To account for competition with HER, we additionally incorporate the HER descriptor and target suppression of HER activity. Given the critical role of reduced B species in nitrogen reduction, an oxidation resistance descriptor is also included, with higher values favoring improved stability against hydroxylation or oxidation. In Figure 7c, Pareto-optimal candidates are labeled, with yellow and blue markers denoting more oxidation-resistant cases. Zr-doped stoichiometric surfaces and Ti-doped B-rich surfaces exhibit higher N_2RR activity and lower HER activity than the parent system. Meanwhile, Fe- and Cr-doped stoichiometric surfaces achieve significantly enhanced N_2RR, albeit with a slight compromise in HER selectivity.

It is important to note that these designed systems are not yet competitive with Cu in CO_2RR or with nitrides in N_2RR, largely because the parent system herein (MoB_2) is intrinsically an exceptionally active HER catalyst. Nevertheless, this analysis highlights the large energy range across different reactions that can be accessed by very dilute doping, and the decorrelated adsorption energetics that enable multiobjective catalyst design.

Looking forward, the most promising research direction lies in understanding and controlling nonuniform, reconstructed, and heterogeneous surface configurations. Rather than targeting a uniform surface dominated by a single type of active site, the design of boride catalysts should aim to engineer a distribution of local motifs—distinct local environments resulting from variations in dopant type/concentration and surface B stoichiometry. Such heterogeneity in surface motifs has the potential to decorrelate reaction energetics, unlock new catalytic pathways, and manipulate conventional activity−selectivity−stability trade-offs across a range of reactions.

CONCLUSIONS

In this work, we have explored the chemical space of surface boron rearrangements and demonstrated how these configurations can be tuned in a controlled way via metal doping and surface boron-enrichment. Extensive ab initio global optimization proves to be a powerful tool for sampling non-stoichiometric reconstructed surfaces, revealing unconventional binding modes and enabling thermodynamic predictions of synthesizable phases. The resulting symmetry-broken, heterogeneous surface phases introduces uncorrelated adsorption modes and energetics, challenging scaling-based catalyst design principles. By performing multiobjective design, we efficiently navigate the uncorrelated energy landscape and identify candidates that escape conventional activity-selectivity-stability trade-offs. Our findings highlight the potential for highly tunable boride catalysts through very dilute doping and suggest that complex, non-mean-field systems represent a new frontier for catalyst design. More broadly, this study provides a generalizable framework for exploiting fluxionality and local structural diversity to engineer advanced catalytic surfaces.

COMPUTATIONAL DETAILS

The hexagonal face of α-phase molybdenum diboride (*P6/mmm*) is modeled by a 6-layer 3 × 3 supercell of (001) termination with a surface area of 71.581 Å. The bottom 3 atomic layers of the slab are constrained as the bulk region, and all others are allowed to relax as the interface region. A vacuum slab of 15 Å is added in the z direction to avoid spurious interactions between periodic images.

The density functional theory (DFT) calculations are performed with the PBE functional[28] and PBE_PAW pseudopotentials[29,30] (H, B, and Mo_pv) using the VASP program (version 5.4.4).[31−34] The D3 correction is added to better account for dispersion interactions.[35] This combination is based on our functional test (Supplementary Note 4) and previous work.[10] The convergence criteria for electronic and force minimization are 10^{-5} eV and 2.0 × 10^{-2} eV/Å, respectively. The Brillouin zone is sampled using Γ-centered 2 × 2 × 1 k-points, and the kinetic energy cutoff for the plane-waves is 500 eV.

The adsorption energies are calculated from the DFT-computed energies via:

$$E_{ads}(X) = E(surf - X) - E(surf) - E(X) \quad (2)$$

where X is H, OH, CO, N, and NH_3. The reference states are gas-phase $\frac{1}{2}H_2$, H_2O-$\frac{1}{2}H_2$, CO, $\frac{1}{2}N_2$, and NH_3, respectively. For the free energetics, we consider zero-point energies and vibrational contributions, all in standard conditions.

All electronic structure analyses are performed based on converged wave functions or charge densities. Bader charges are computed using the Bader Charge Analysis program.[36] The transition states are located using the nudged elastic band method.[37]

The global optimization minima searches are performed using our open-sourced *Python* package, `GOCIA`.[19] The structures of the undoped and doped surfaces, with varying amounts of surface boron, are sampled with the box-sampling method. The most stable adsorption configurations are sampled with the fragment-based box-sampling approach. No fixed lattices or connectivities are assumed during the sampling. More details are in Supplementary Note S1.

Ab initio molecular dynamics simulations are performed using the same DFT methods as mentioned, except for a lower kinetic energy cutoff of 400 eV. The simulations are performed within the *NVT* ensemble at 300 K with a Nosé-Hoover thermostat.[38,39] The simulations are run with a time step of 1 fs, and a 10 ps trajectory is collected after pre-equilibration for analysis.

ASSOCIATED CONTENT

Data Availability Statement

All global and local minima structures from the global optimization minima searches are available on the catalysis-hub.org repository[40] at data entry#`ZhangDopant-dependent2025`. Full ensemble files, Bader charges, and

https://doi.org/10.1021/acscatal.5c08265
ACS Catal. 2026, 16, 1729−1737

GOCIA inputs are available on Zenodo at https://doi.org/10.5281/zenodo.18136681.

Supporting Information

The Supporting Information is available free of charge at https://pubs.acs.org/doi/10.1021/acscatal.5c08265.

The details of the grand canonical global optimizations, the stability of the surface phases, the Pareto search scheme for the multiobjective design, and the test of density functional methods; statistics of the sampling of nonstoichiometric doped surfaces; visualization of the larger-scale periodic pattern of the surface boron layers; structures of all accessible surface phases; the energy difference between configurations i and ii for non-stoichiometric doped surfaces and their correlation with dopant properties; ab initio molecular dynamics simulations; Bader charge of surface atoms of all accessible surface phases; statistics of the sampling of adsorption configurations; and structures of all global minima adsorption configurations (PDF)

AUTHOR INFORMATION

Corresponding Author

Frank Abild-Pedersen − *SUNCAT Center for Interface Science and Catalysis, SLAC National Accelerator Laboratory, Menlo Park, California 94025, United States;* orcid.org/0000-0002-1911-074X; Email: abild@slac.stanford.edu

Author

Zisheng Zhang − *SUNCAT Center for Interface Science and Catalysis, SLAC National Accelerator Laboratory, Menlo Park, California 94025, United States; Department of Chemical Engineering, Stanford University, Stanford, California 94305, United States*

Complete contact information is available at: https://pubs.acs.org/10.1021/acscatal.5c08265

Notes

The authors declare no competing financial interest.

ACKNOWLEDGMENTS

Z.Z. is supported by the Stanford Energy Fellowship and the Precourt Institute for Energy, Doerr School of Sustainability. F.A-P. acknowledges support from the U.S. Department of Energy, Office of Science, Office of Basic Energy Sciences, Chemical Sciences, Geosciences, and Biosciences Division, Catalysis Science Program through the SUNCAT Center for Interface Science and Catalysis. Computational facilities used to conduct this study include S3DF, the SLAC Shared Scientific Data Facility; Sherlock, a university-shared computing cluster operated by the Stanford Research Computing Center; and the National Energy Research Scientific Computing Center, a DOE Office of Science User Facility supported by the Office of Science of the U.S. Department of Energy under Contract No. DE-AC02-05CH11231 using NERSC award BES-ERCAP0024127. Z.Z. thanks Thomas F. Jaramillo, Junjie Chen, and Alfred Vargas for helpful discussions and Kirsten Winther for assistance in uploading the datasets.

REFERENCES

(1) Zubarev, D. Y.; Boldyrev, A. I. Developing paradigms of chemical bonding: adaptive natural density partitioning. *Physical chemistry chemical physics* **2008**, *10*, 5207−5217.

(2) Li, W.-L.; Chen, X.; Jian, T.; Chen, T.-T.; Li, J.; Wang, L.-S. From planar boron clusters to borophenes and metalloborophenes. *Nat. Rev. Chem.* **2017**, *1*, No. 0071.

(3) Pan, S.; Barroso, J.; Jalife, S.; Heine, T.; Asmis, K. R.; Merino, G. Fluxional Boron Clusters: From Theory to Reality. *Acc. Chem. Res.* **2019**, *52*, 2732−2744.

(4) Lee, E.; Fokwa, B. P. Nonprecious metal borides: Emerging electrocatalysts for hydrogen production. *Acc. Chem. Res.* **2022**, *55*, 56−64.

(5) Hong, J.; Mutalik, S.; Pescarmona, P. P.; Protesescu, L. Metal Borides: From Industrial Classics to Versatile Colloidal Nanocrystals for Energy, Catalysis, and Hard Coatings Applications. *Chem. Mater.* **2024**, *36*, 2147−2164.

(6) Venegas, J. M.; McDermott, W. P.; Hermans, I. Serendipity in catalysis research: boron-based materials for alkane oxidative dehydrogenation. *Accounts of chemical research* **2018**, *51*, 2556−2564.

(7) Park, H.; Encinas, A.; Scheifers, J. P.; Zhang, Y.; Fokwa, B. P. Boron-dependency of molybdenum boride electrocatalysts for the hydrogen evolution reaction. *Angew. Chem., Int. Ed.* **2017**, *56*, 5575−5578.

(8) Goto, T.; Ito, S.-i.; Shinde, S. L.; Ishibiki, R.; Hikita, Y.; Matsuda, I.; Hamada, I.; Hosono, H.; Kondo, T. Carbon Dioxide Adsorption and Conversion to Methane and Ethane on Hydrogen Boride Sheets. *Commun. Chem.* **2022**, *5*, 118.

(9) Zhang, Z.; Hermans, I.; Alexandrova, A. N. Off-stoichiometric Restructuring and Sliding Dynamics of Hexagonal Boron Nitride Edges in Conditions of Oxidative Dehydrogenation of Propane. *J. Am. Chem. Soc.* **2023**, *145*, 17265−17273.

(10) Zhang, Z.; Abild-Pedersen, F. Off-Equilibrium Reactivity of Boron-Enriched Metal Diboride Surfaces in Electroreduction Conditions. *ACS Catal.* **2025**, *15*, 12340−12350.

(11) Kawashima, K.; Márquez, R. A.; Smith, L. A.; Vaidyula, R. R.; Carrasco-Jaim, O. A.; Wang, Z.; Son, Y. J.; Cao, C. L.; Mullins, C. B. A review of transition metal boride, carbide, pnictide, and chalcogenide water oxidation electrocatalysts. *Chem. Rev.* **2023**, *123*, 12795−13208.

(12) Zhang, A.; Liang, Y.; Zhang, H.; Geng, Z.; Zeng, J. Doping Regulation in Transition Metal Compounds for Electrocatalysis. *Chem. Soc. Rev.* **2021**, *50*, 9817−9844.

(13) Barroso, J.; Pan, S.; Merino, G. Structural transformations in boron clusters induced by metal doping. *Chem. Soc. Rev.* **2022**, *51*, 1098−1123.

(14) Zhang, Z.; Jimenez-Izal, E.; Hermans, I.; Alexandrova, A. N. Dynamic phase diagram of catalytic surface of hexagonal boron nitride under conditions of oxidative dehydrogenation of propane. *journal of physical chemistry letters* **2019**, *10*, 20−25.

(15) Cendejas, M. C.; Paredes Mellone, O. A.; Kurumbail, U.; Zhang, Z.; Jansen, J. H.; Ibrahim, F.; Dong, S.; Vinson, J.; Alexandrova, A. N.; Sokaras, D.; et al. Tracking Active Phase Behavior on Boron Nitride during the Oxidative Dehydrogenation of Propane Using Operando X-Ray Raman Spectroscopy. *J. Am. Chem. Soc.* **2023**, *145*, 25686−25694.

(16) Jothi, P. R.; Zhang, Y.; Scheifers, J. P.; Park, H.; Fokwa, B. P. T. Molybdenum diboride nanoparticles as a highly efficient electrocatalyst for the hydrogen evolution reaction. *Sustainable Energy Fuels* **2017**, *1*, 1928−1934.

(17) Li, S.; Gunda, H.; Ray, K. G.; Wong, C.-S.; Xiao, P.; Friddle, R. W.; Liu, Y.-S.; Kang, S.; Dun, C.; Sugar, J. D.; et al. Spontaneous dynamical disordering of borophenes in MgB2 and related metal borides. *Nat. Commun.* **2021**, *12*, 6268.

(18) Jothi, P. R.; Yubuta, K.; Fokwa, B. P. A simple, general synthetic route toward nanoscale transition metal borides. *Adv. Mater.* **2018**, *30*, No. 1704181.

(19) Zhang, Z.; Gee, W.; Lavroff, R. H.; Alexandrova, A. N. GOCIA: a grand canonical global optimizer for clusters, interfaces, and adsorbates. *Phys. Chem. Chem. Phys.* **2025**, *27*, 696−706.

(20) Portehault, D.; Devi, S.; Beaunier, P.; Gervais, C.; Giordano, C.; Sanchez, C.; Antonietti, M. A general solution route toward metal boride nanocrystals. *Angewandte Chemie-German Edition* **2011**, *123*, 3320.
(21) Robinson, P. J.; Munarriz, J.; Valentine, M. E.; Granmoe, A.; Drichko, N.; Chamorro, J. R.; Rosa, P. F.; McQueen, T. M.; Alexandrova, A. N. Dynamical Bonding Driving Mixed Valency in a Metal Boride. *Angew. Chem., Int. Ed.* **2020**, *59*, 10996−11002.
(22) Zhang, Z.; Zandkarimi, B.; Alexandrova, A. N. Ensembles of metastable states govern heterogeneous catalysis on dynamic interfaces. *Accounts of chemical research* **2020**, *53*, 447−458.
(23) Nitopi, S.; Bertheussen, E.; Scott, S. B.; Liu, X.; Engstfeld, A. K.; Horch, S.; Seger, B.; Stephens, I. E.; Chan, K.; Hahn, C.; Nørskov, J. K.; Jaramillo, T. F.; Chorkendorff, I. Progress and Perspectives of Electrochemical CO2 Reduction on Copper in Aqueous Electrolyte. *Chem. Rev.* **2019**, *119*, 7610−7672.
(24) Légaré, M.-A.; Bélanger-Chabot, G.; Dewhurst, R. D.; Welz, E.; Krummenacher, I.; Engels, B.; Braunschweig, H. Nitrogen Fixation and Reduction at Boron. *Science* **2018**, *359*, 896−900.
(25) Ruddy, A. J.; Ould, D. M. C.; Newman, P. D.; Melen, R. L. Push and Pull: The Potential Role of Boron in N2 Activation. *Dalton Transactions* **2018**, *47*, 10377−10381.
(26) Logadottir, A.; Rod, T.; Nørskov, J.; Hammer, B.; Dahl, S.; Jacobsen, C. The Brønsted−Evans−Polanyi Relation and the Volcano Plot for Ammonia Synthesis over Transition Metal Catalysts. *J. Catal.* **2001**, *197*, 229−231.
(27) Montoya, J. H.; Tsai, C.; Vojvodic, A.; Nørskov, J. K. The Challenge of Electrochemical Ammonia Synthesis: A New Perspective on the Role of Nitrogen Scaling Relations. *ChemSusChem* **2015**, *8*, 2180−2186.
(28) Perdew, J. P.; Burke, K.; Ernzerhof, M. Generalized gradient approximation made simple. *Physical review letters* **1996**, *77*, 3865.
(29) Kresse, G.; Joubert, D. From ultrasoft pseudopotentials to the projector augmented-wave method. *Physical review b* **1999**, *59*, 1758.
(30) Blöchl, P. E. Projector augmented-wave method. *Phys. Rev. B* **1994**, *50*, 17953.
(31) Kresse, G.; Hafner, J. Ab initio molecular dynamics for liquid metals. *Phys. Rev. B* **1993**, *47*, 558−561.
(32) Kresse, G.; Hafner, J. Ab initio molecular-dynamics simulation of the liquid-metal−amorphous-semiconductor transition in germanium. *Phys. Rev. B* **1994**, *49*, 14251−14269.
(33) Kresse, G.; Furthmüller, J. Efficient iterative schemes for ab initio total-energy calculations using a plane-wave basis set. *Phys. Rev. B* **1996**, *54*, 11169−11186.
(34) Kresse, G.; Furthmüller, J. Efficiency of ab-initio total energy calculations for metals and semiconductors using a plane-wave basis set. *Comput. Mater. Sci.* **1996**, *6*, 15−50.
(35) Grimme, S.; Antony, J.; Ehrlich, S.; Krieg, H. A consistent and accurate ab initio parametrization of density functional dispersion correction (DFT-D) for the 94 elements H-Pu. *J. Chem. Phys.* **2010**, *132*, 154104.
(36) Yu, M.; Trinkle, D. R. Accurate and efficient algorithm for Bader charge integration. *J. Chem. Phys.* **2011**, *134*, No. 064111.
(37) Mills, G.; Jónsson, H.; Schenter, G. K. Reversible work transition state theory: application to dissociative adsorption of hydrogen. *Surf. Sci.* **1995**, *324*, 305−337.
(38) Shuichi, N. Constant temperature molecular dynamics methods. *Prog. Theor. Phys. Suppl.* **1991**, *103*, 1−46.
(39) Hoover, W. G. Canonical dynamics: Equilibrium phase-space distributions. *Phys. Rev. A* **1985**, *31*, 1695.
(40) Winther, K. T.; Hoffmann, M. J.; Boes, J. R.; Mamun, O.; Bajdich, M.; Bligaard, T. Catalysis-Hub. org, an open electronic structure database for surface reactions. *Sci. Data* **2019**, *6*, 75.

https://doi.org/10.1021/acscatal.5c08265
ACS Catal. 2026, 16, 1729−1737